AFRL-SN-HS-TR-2004-026

UHF STRIP – SAR AND ISAR IMAGES OF A TANK: APPLICATION OF SCALE – MODEL MEASUREMENTS

Dr. J. Leon Poirier   ARCON Corporation
Dr. James Ernstmeyer   AFRL/SNHE
Dr. Peter Franchi   ARCON Corporation
1st Lt Chet Ouch   AFRL/SNHE
Dr. John K. Schindler   Veridian Corporation
Mr. Elihu J. Tichovolsky   AFRL/SNHE

IN HOUSE REPORT – APRIL 2002 – APRIL 2003

APPROVED FOR PUBLIC RELEASE: DISTRIBUTION UNLIMITED
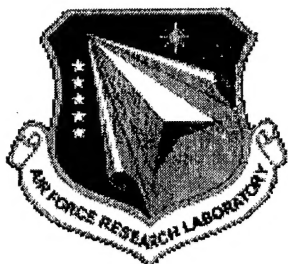
20040623 009

IN HOUSE REPORT

Title: UHF Strip-SAR and ISAR Images of a Tank:
Application of Scale-Model Measurements

PUBLICATION REVIEW

THIS TECHNICAL REPORT HAS BEEN REVIEWED AND IS APPROVED FOR PUBLICATION:

APPROVED:

BERTUS WEIJERS
Branch Chief
Electromagnetic Scattering Branch

APPROVED/DISAPPROVED
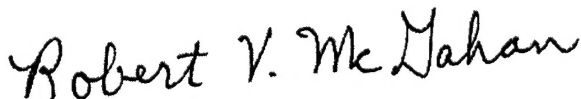
ROBERT V. McGAHAN
Technical Advisor
Electromagnetic Technology Division

REPORT DOCUMENTATION PAGE

Form Approved
OMB No. 0704-0188

maintaining the data needed, and completing and reviewing this collection of information. Send comments regarding this burden estimate or any other aspect of this collection of information, including suggestions for reducing this burden to Department of Defense, Washington Headquarters Services, Directorate for Information Operations and Reports (0704-0188), 1215 Jefferson Davis Highway, Suite 1204, Arlington, VA 22202-4302. Respondents should be aware that notwithstanding any other provision of law, no person shall be subject to any penalty for failing to comply with a collection of information if it does not display a currently valid OMB control number. **PLEASE DO NOT RETURN YOUR FORM TO THE ABOVE ADDRESS.**

1. REPORT DATE (DD-MM-YYYY) 16-10-2003	2. FINAL REPORT	3. DATES COVERED (From - To) April 2002 – April 2003

4. TITLE AND SUBTITLE
UHF Strip – SAR and ISAR Images of a Tank: Application of Scale – Model Measurements

5a. CONTRACT NUMBER

5b. GRANT NUMBER

5c. PROGRAM ELEMENT NUMBER
62204F

6. AUTHOR(S)
Dr. J. Leon Poirier   Elihu J. Tichovolsky
Dr. James Ernstmeyer
Dr. Peter Franchi
1st Lt. Chet Ouch
Dr. John K. Schindler

5d. PROJECT NUMBER
4916

5e. TASK NUMBER
HE

5f. WORK UNIT NUMBER
01

7. PERFORMING ORGANIZATION NAME(S) AND ADDRESS(ES)
ARCON Corporation. 260 Bear Hill Road. Waltham MA 02154
AFRL/SNHE, 80 Scott Drive, Hanscom AFB MA 01731-2909
Veridian Corporation, 3040 Williams Drive, Suite 200 Fairfax , VA 22031

8. PERFORMING ORGANIZATION REPORT

9. SPONSORING / MONITORING AGENCY NAME(S) AND ADDRESS(ES)
Electromagnetics Technology Division
Sensors Directorate
AFRL/SNHE
80 Scott Drive
Hanscom AFB MA 01731-2909

10. SPONSOR/MONITOR'S ACRONYM(S)

AFRL/SNHE

11. SPONSOR/MONITOR'S REPORT NUMBER(S)

12. DISTRIBUTION / AVAILABILITY STATEMENT

APPROVED FOR PUBLIC RELEASE; DISTRIBUTION IS UNLIMITED

13. SUPPLEMENTARY NOTES

14. ABSTRACT
    UHF images of a tank on the ground were obtained by measuring a scale model of the tank on a ground plane. With a scale factor of 35, the laboratory radar range frequencies of 6 to 18 GHz scale to 171.4 to 514.3 MHz. The dielectric constant of the ground plane material was matched to that of the real ground to insure that the images of the full-scale tank matched those of a full-scale tank.
    We found that the correlation between images at the same aspect falls off rapidly even for differences in grazing angle of a few degrees. We converted the measured ISAR images to strip-SAR format as would be obtained by an airborne UHF SAR. The correlation between the ISAR and strip-SAR images is high. The correlation, however, falls off as the grazing angle and synthetic aperture length increase.
    Scale model measurements offer an approach to obtaining multi-aspect images of military targets that are quick and cost effective compared to full scale airborne or turntable measurements. Scale models of a wide array of military vehicles are readily available. Nonmetallic objects such as the ground and vegetation are fabricated from materials that have the same dielectric properties as a function of the scaled X-band laboratory measurement frequency as do the full-scale objects at UHF. This insures that the measurement yield accurate representations of the RCS and images of the full-scale objects.

15. SUBJECT TERMS
Foliage Penetration Radar, UHF Radar Cross- Section of Vehicular Targets, UHF Radar Images of Vehicular Targets, Model Measurements.

16. SECURITY CLASSIFICATION OF: Unclassified			17. LIMITATION OF ABSTRACT	18. NUMBER OF PAGES	19a. NAME OF RESPONSIBLE PERSON Bertus Weijers
a. REPORT Unclassified	b. ABSTRACT Unclassified	c. THIS PAGE Unclassified	Indicate if it is UNC		19b. TELEPHONE NUMBER (include area code) 781-377-2987

Standard Form 298 (Rev. 8-98)
Prescribed by ANSI Std. Z39.18

Contents

Illustrations

Tables

Preface

1.   INTRODUCTION

Obtaining images of vehicular targets from airborne synthetic aperture radars (SAR) under a variety of controlled conditions is difficult and costly. Practical and economic constraints involved in flight test programs limit the number of target aspects, grazing angles, and soil types that can be investigated. Development of robust target discrimination algorithms requires target images at many closely spaced angles to train and evaluate the algorithms. Most target discrimination and classification algorithms compare an unknown target image with previously-obtained known target images. If the match between the current image and the known image is sufficiently close, the target is declared to be the known comparison target with some measure of confidence. The performance of such image comparison algorithms generally improves with the number of known target poses against which to compare the unknown target image.

The images needed at different aspects and for different soil types, grazing angles, and targets, where airborne data are not available, must be obtained by other methods. Three methods that can be used are (1) mathematical extrapolation of an existing image at one aspect to one at another aspect, (2) full-size turntable measurements, and (3) scale-model measurements. Each of these approaches has advantages and limitations. We present UHF images of a tank obtained from scale-model measurements and discuss the applicability of scale-model measurements to derive VHF/UHF images and radar cross section (RCS) of vehicular targets under various conditions. Laboratory scale-model measurements produce high quality images at all aspect angles, poses, grazing angles, and soil types more quickly and cost effectively than full-scale airborne or turntable measurements.

2. SCALE-MODEL MEASUREMENTS

The key factors making scale-model measurements attractive are the relatively long wavelengths and poorer resolution of synthetic aperture radars in the VHF/UHF bands that render target details that are small compared to radar wavelength unimportant. Therefore, scaled VHF/UHF targets are much easier to fabricate. They are also inexpensive. In fact, our targets are plastic models that are readily available for virtually any piece of foreign and U.S. military equipment in existence. After assembly, the models are covered with a conducting material to a thickness sufficient to give them the correct electrical properties at the laboratory measurement frequencies. We use 1/35-, 1/72-, and 1/87-scale models depending on the frequency band to be scaled.

Techniques for the measurement of conducting models to determine the RCS and images of the corresponding full-size targets were established decades ago. The RCS of a full-size conducting object of characteristic dimension D_o illuminated by a signal of frequency f_o can be

1

determined by substituting a scale model of the object of characteristic dimension $D_1 = D_o/Q$ at a frequency $f_1 = Qf_o$ where Q is the scale factor, that is 35 for the data presented in this report. Then, the RCS of the full-size target Σ is given by $\Sigma = Q^2\Sigma_1$ where Σ_1 is the measured RCS of the model.[1]

To apply this technique to dielectric objects and the ground plane beneath the model target, it is necessary that the complex electrical properties, permittivity ε_r, permeability μ_r, and conductivity σ, of the object at the model measurement frequency f_1 be the same as those of the full-size object at f_o, viz., $\varepsilon_{r1} = \varepsilon_{ro}$, $\mu_1 = \mu_o$, and $\sigma_1 = Q\sigma_o$.[2] For RCS measurements, it is sufficient to match the real and imaginary parts of the material properties at the frequency where the RCS is desired. For images, the match must extend over the entire bandwidth of the laboratory measurement signal. The University of Massachusetts Lowell (UML) Expert Radar Signatures (ERADS) group has pioneered techniques, verified with numerous measurements on a wide variety of target types, for fabricating dielectric materials for such measurements.[3,4] Epoxy resins, plastics, and waxes are loaded with aluminum powder, carbon powder, carbon fibers, and other amendments to produce scale-dielectric materials that display, at the higher laboratory measurement frequency, the same dielectric properties as their full-size counterparts at the lower real-world frequencies.

3. MEASUREMENT RANGE
The measurements reported here were made at the University of Massachusetts ERADS facility at Lowell, MA[5] using a computer-controlled measurement system consisting of an HP8510B vector network analyzer coupled to a dual-polarized quad-ridge horn followed by a 12-inch diameter hyperbolic/plano dielectric lens. Two motor-driven pylon translation/rotation stages hold the ground plane on which the target object is mounted and the calibration target, respectively. The transmitted signal sweeps from 6 to 18 GHz in 256 discrete steps. The scale factor of 35, appropriate for the 1/35-scale models, translates the measurement results from X-band to the full-scale frequencies of 171.4 to 514.3 MHz. Measurements were made at two polarizations, HH and VV, although the VH and HV polarizations could also have been measured. The tilt angle of the rotating ground plane is adjustable to provide grazing angles of 20 – 60 degrees. The grazing angles for the measurements reported here, however, ranged only from 27 to 33 degrees. During a data collections run, the in-phase and quadrature-phase (I & Q) components of the scattered signal are recorded at each discrete frequency step and for each degree of aspect angle from 0 – 360 degrees. The system is continually calibrated with an

---

[1] Currie, Nicholas C., Editor, *Radar Reflectivity Measurement Techniques and Applications*, Artech House, Boston, London 1989

[2] Sinclair, George, "Theory of Models of Electromagnetic Systems," PROC. IRE, pp. 1364-1370, Nov. 1948

[3] Giles, R.H, Gatesman, A. J., Fitz-Gerald, J., Fisk, S. and Waldman, J. "Tailoring Artificial Dielectric Materials at Terahertz /Frequencies," The Fourth International Symposium on Space Terahertz Technology, April 1993, Los Angeles, CA

[4] Bober, Kenneth M., Giles, Robert H, and Waldman, Jerry "Tailoring The Microwave Permittivity And Permeability Of Composite Materials," Submillimeter-Wave Technology Center, University of Massachusetts, Lowell, MA

[5] Beaudoin, Christopher J., "Development of a 1/35th Scale VHF/UHF Far-Field RCS imaging System Used To Investigate Scattering and Imagery of Tree Obscured Targets," Master of Science Thesis, Dept. of Electrical Engineering, University of Massachusetts, Lowell, MA

optically-aligned standard. A photograph of the tank model on the ground plane is shown in Figure 1.
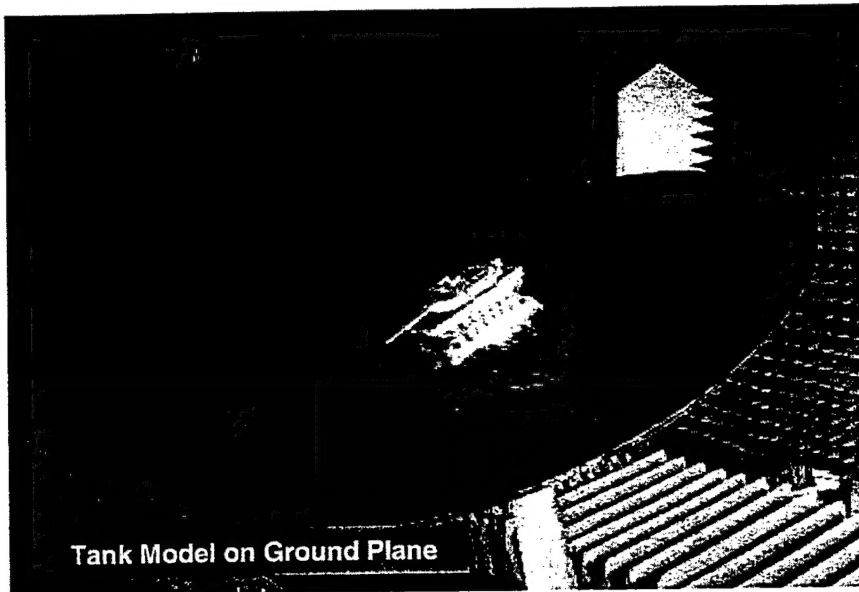

Figure 1. Photograph of a Tank Model on Ground Plane. Dielectric ground plane was covered with conducting foil for calibration test.

The I & Q data are processed to obtain RCS versus aspect angle at each of the 256 stepped sample frequencies. These data are also used to form ISAR images at any aspect from 0 to 360 degrees. The range resolution and cross-range resolutions depend, respectively, on the frequency bandwidth and synthetic aperture length used in forming the images. Both of these can be varied to create images of different resolutions from the same data set. A resolution cell size of about 1 x 1 meter at the full-scale frequency is typical. Aliasing is controlled by the sampling rate over the bandwidth and aperture. An important advantage of scale-model target measurements is that unlike airborne measurements that yield an image at only a single aspect for each pass, a single model measurement run yields images at all aspects. Furthermore, we can change the grazing angle by simply changing the tilt angle of the ground plane. To investigate the impact of different ground plane dielectric constants, we replace the ground plane with one of different complex permittivity.

4. GROUND PLANE CONSIDERATIONS

The radar signal scattered from a target depends on the ground upon which it rests. This is because energy reflected from the foreground toward the target can be reflected by the target back to the radar. In the presence of this dihedral multipath scattering, the signal actually reaching the target is the coherent (complex) sum of the direct path signal and that reflected from the foreground. The signal that actually reaches the radar is the sum of four distinct components: the direct signal that suffers no foreground reflection, two components that suffer a single foreground reflection, and a final component that suffers two foreground reflections. In practice, the single foreground-reflected dihedral component of the signal, when present, often dominates the observed RCS of a target and nearby trees. Therefore, to obtain accurate measurements of RCS and high fidelity images of targets, the laboratory ground plane upon which the model is

3

placed must match the electrical properties of the soil where the full-size target image is measured.

For our measurements, we formulated the dielectric properties of the ground plane at the X-band laboratory measurement frequency to match those typical of fairly moist soil at UHF. Figure 2 shows the real and imaginary parts of the soil dielectric constant for four moisture contents. It is apparent that the real part of the dielectric constant increases rapidly with soil moisture and is not strongly dependent on frequency over the range 50 – 500 MHz. By contrast, the imaginary part of the dielectric constant for moist soil, although much smaller than the real part, tends to decrease as the frequency increases. For these measurements, we fabricated a ground plane four feet in diameter with a nominal dielectric constant of $\varepsilon_r = 13.9 - j2.3$, corresponding to a moisture content of about 30%.
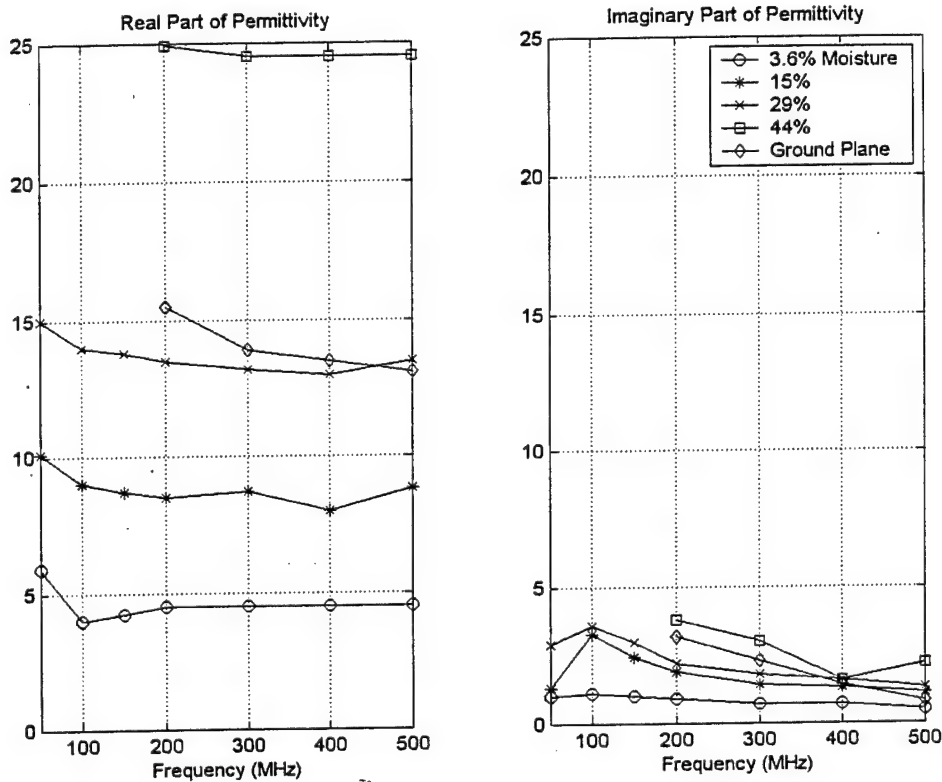
Figure 2. Complex Permittivity of Laboratory Ground Plane and Soil
For Four Soil Moisture Contents

The severity of the foreground dihedral multipath scattering depends on the grazing angle and the soil's dielectric constant and roughness. Usually, the double-bounce return, having lost energy twice in reflecting off the ground, can be ignored compared to the direct and single bounce components. The single bounce return will often dominate the total return especially for steep grazing angles and targets of large vertical extent. Furthermore, the single bounce dihedral return is not a sensitive function of grazing angle and tends to produce a large return over a broad range of elevation angles away from the Brewster angle. However, surface roughness can reduce the specular reflection from the foreground dramatically and greatly decrease the dihedral reflection component. Another factor that impacts the dihedral reflection process is the angle

4

between the reflecting surface on the target and the foreground surface. When the two surfaces are not perpendicular, the intensity of the multipath contribution decreases significantly or vanishes.

The Fresnel reflection coefficient of the foreground determines the potential for strong multipath interaction. Figure 3 shows the magnitudes of the Fresnel reflection coefficients for two soils, one very dry (less than 3% moisture) and one moist (about 30% moisture, i.e., the same as our ground plane).
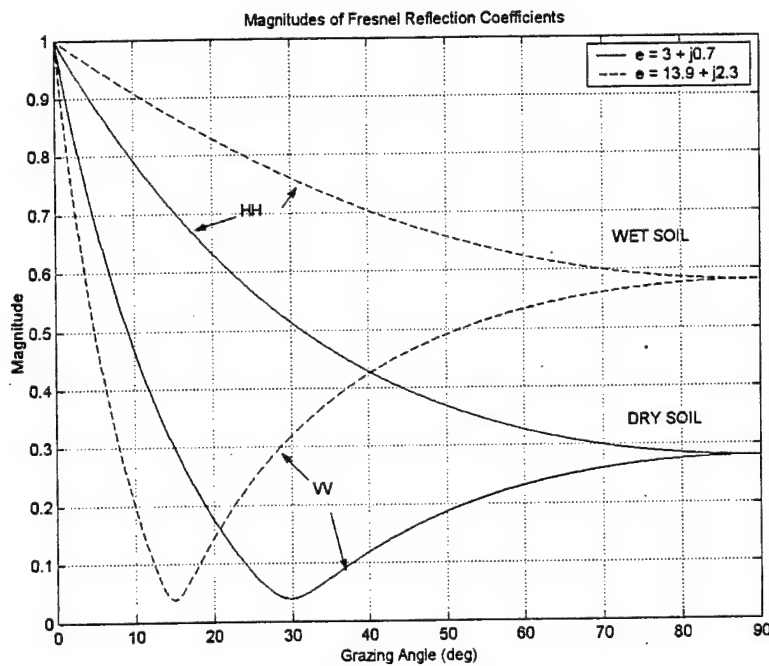

Figure 3. Magnitudes of Fresnel Reflection Coefficients for Two Soil Moistures

The curves show marked differences in the reflection coefficients of the dry and moist soils. For a given moisture content, the HH reflection coefficient is always larger than the VV value. For an object with the same VV and HH free-space RCS, the single-bounce contribution to the cross section will be higher for HH polarization than for VV polarization by the factor $(\Gamma_{HH}/\Gamma_{VV})^2$ where Γ_{HH} and Γ_{VV} are the magnitudes of the HH and VV Fresnel reflection coefficients, respectively. The null in the VV coefficients, where the reflections are least, occur at the Brewster angle $\theta_B = \sin^{-1}\left(\sqrt{\varepsilon_r/(1+\varepsilon_r)}\right)$. The grazing angle at which the null occurs varies widely with moisture content and the variation in the reflection coefficient with angle is greatest in that region. The out-and-back single-bounce contribution, both components, to the RCS is $4\Gamma_{VV}^2\sigma_B$, where Γ_{VV} is the magnitude of the Fresnel reflection coefficient and σ_B is the target bistatic cross section at the grazing angle.

In Figure 4 we show the difference $\Delta_i = 20\log(\Gamma_{iD}/\Gamma_{iM})$ between the single-bounce contributions to the RCS of a scatterer for the two soil moistures shown in Figure 3. Here i is VV or HH and M and D indicate moist and dry soil, respectively. Figure 4 shows the wide variation in the single-bounce term that would be observed for the two soil conditions as a function of the grazing angle.

Ground roughness also affects the severity of the multipath. As the ground becomes rougher, the reflection process becomes less specular and more diffuse. This reduces the effective value of the Fresnel reflection coefficient and diminishes any multipath effects. For a given ground roughness, the reduction of the refection coefficient increases with frequency. Once the ground roughness is on the order of the wavelength, the specular part of the reflection coefficient is negligible and multipath effects are not important.

The RCS and image of a target will be affected by the permittivity and roughness of the terrain under and immediately in front of the target vehicle. Therefore, classification algorithms will be stressed when ground conditions are different from the test conditions used to obtain the training data. This is why it is important to match the model measurement parameters as closely as possible to those of the full-size scene, also, this is why scale-model measurements are such a valuable tool. Unlike airborne or full-size turntable measurements, the dielectric properties and roughness of the ground plane under the target can be controlled and changed at will to produce images over a wide range of conditions.
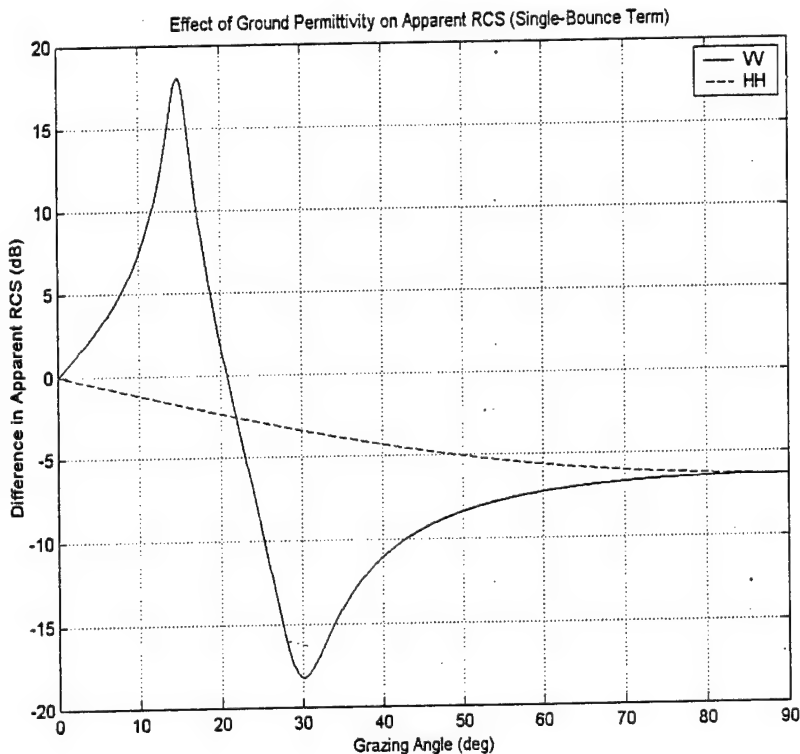

Figure 4. Difference, $\Delta_i = 20\log(\Gamma_{iD}/\Gamma_{iM})$, in Apparent RCS of Single-Bounce Term for the Two Soil Moistures in Figure 3. $i = VV$ and HH.

6

5. MODEL MEASUREMENT RESULTS

5.1 UHF RCS of a Tank

In this section we present the RCS data obtained for the 1/35-scale model tank. The model was placed on a ground plane 48 inches in diameter with a nominal dielectric constant of $\varepsilon_r = 13.9 - j2.3$. The data were collected at 256 discrete frequencies at one-degree increments of aspect angle from 0 to 180 deg and constant grazing angle of 30 deg. We restricted the azimuth angle range to 180 deg even though the tank target is not exactly symmetrical. The entire 360-deg range was not necessary to achieve the goals of this report. Thirteen runs were made for grazing angles of 27 to 33 degrees in increments of 0.5 deg. Photographs of the tank model taken for five aspects and 30 degrees elevation are shown in Figure 5. These are useful in understanding not only the RCS variation but also, the variation of the images with aspect presented in the next section.

The radar cross section of a tank as a function of azimuth angle for a grazing angle of 30 deg is shown in Figures 6 and 7 for 12 frequencies from 200 to 475 MHz. As expected, the periodicity of the RCS variations increases with signal frequency. RCS maxima occur at broadside and end-on aspects, 90 deg and 0/360 deg, respectively. In the broadside pose, the tank presents its largest possible projected area and, therefore, its largest RCS ranging between about 25 and 30 dBsm. Also, the apparent HH RCS for all frequencies and nearly all aspects is larger than the VV RCS. There are substantial changes in the fine structure of the RCS versus aspect angle pattern with frequency. This is due to relative phases of the contributions from different scattering centers of the target and the relative phases of the direct and single bounce terms changing with frequency. Constructive and destructive interference among these components produces the changes in the observed RCS.

7
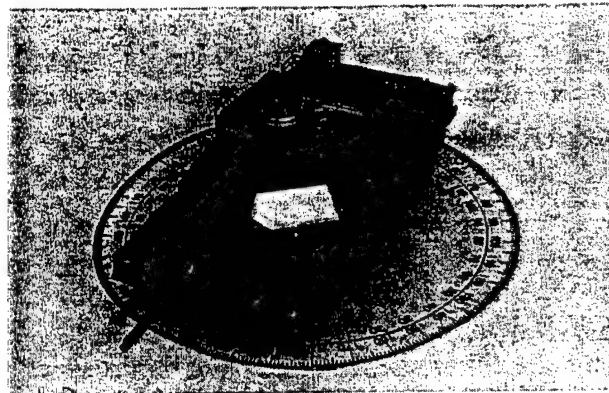
30 Deg Aspect, 30 Deg Elevation
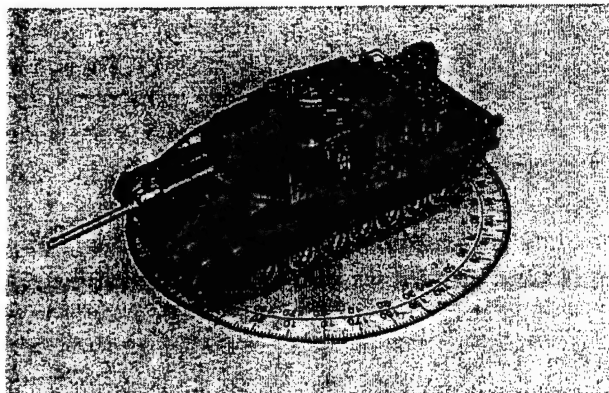
60 Deg Aspect, 30 Deg Elevation
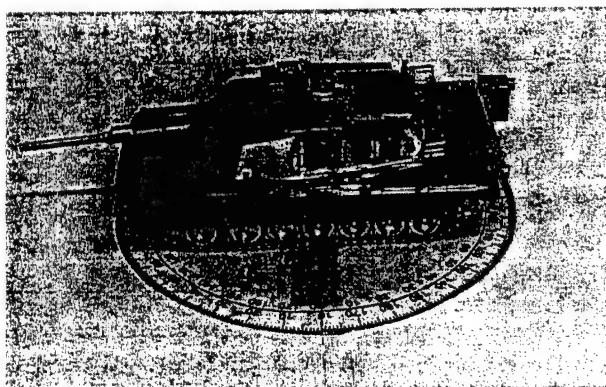
90 Deg Aspect, 30 Deg Elevation
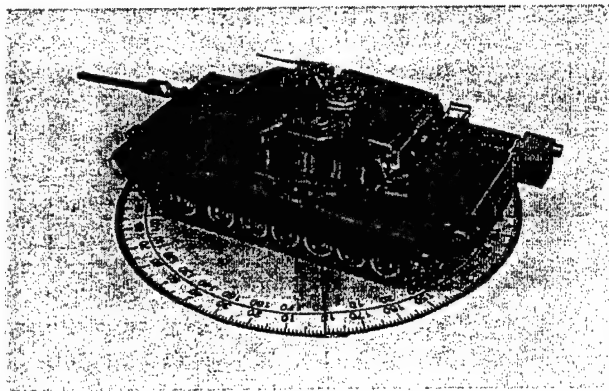
120 Deg Aspect, 30 Deg Elevation
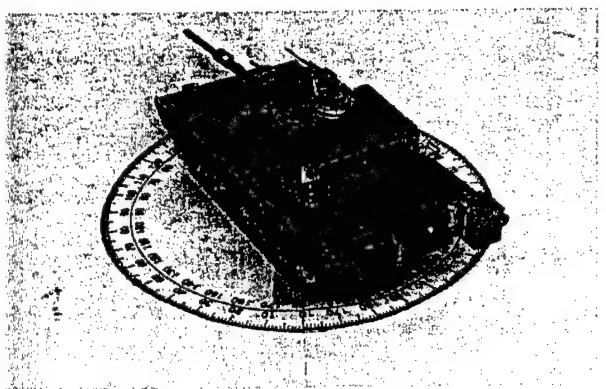
150 Deg Aspect, 30 Deg Elevation

Figure 5. Photographs of Tank Model Taken at Five Aspects.
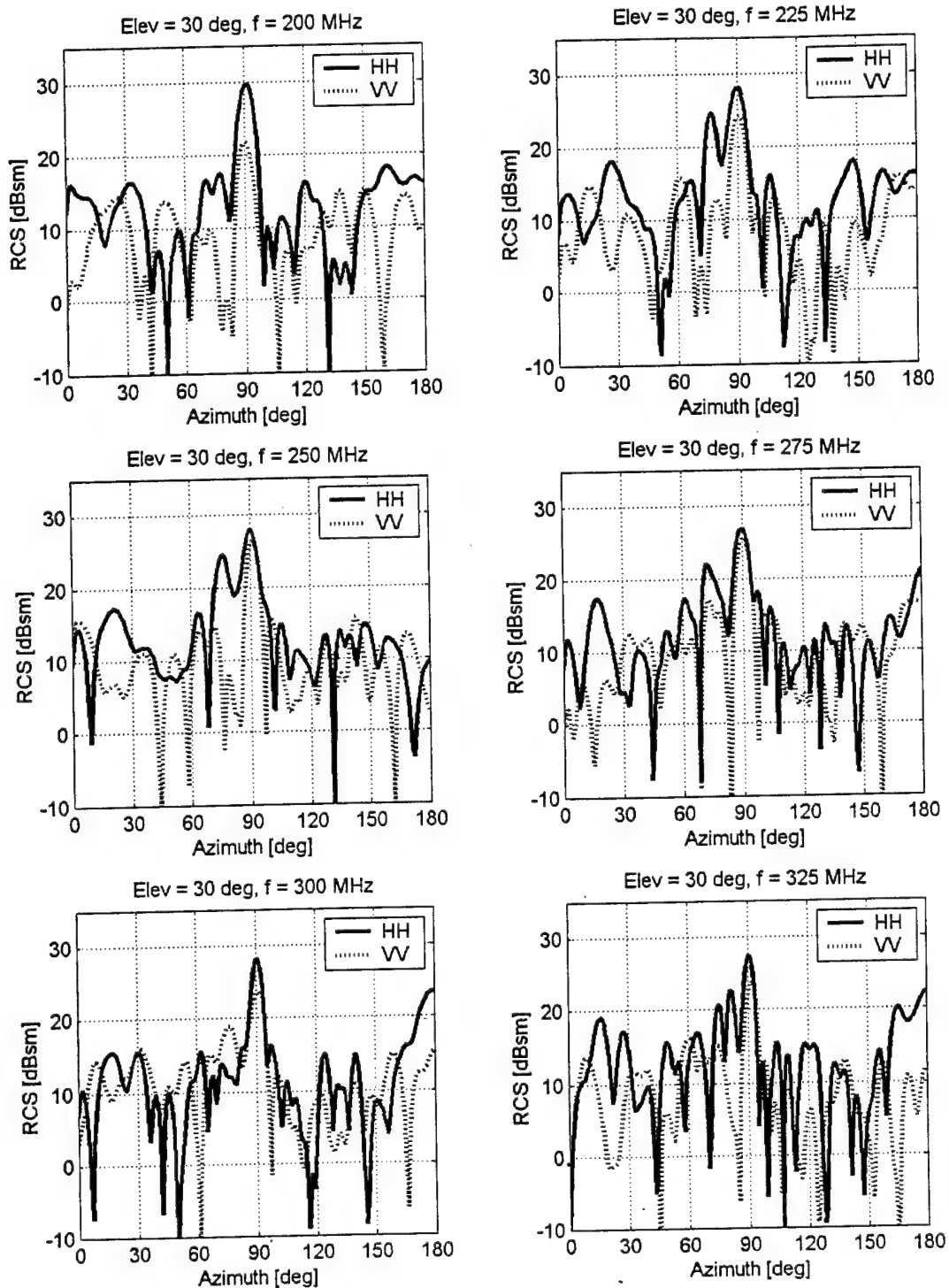
Figure 6. RCS of Full-size Tank Obtained from Model Measurements at 200, 225, 250, 275, 300, and 325 MHz
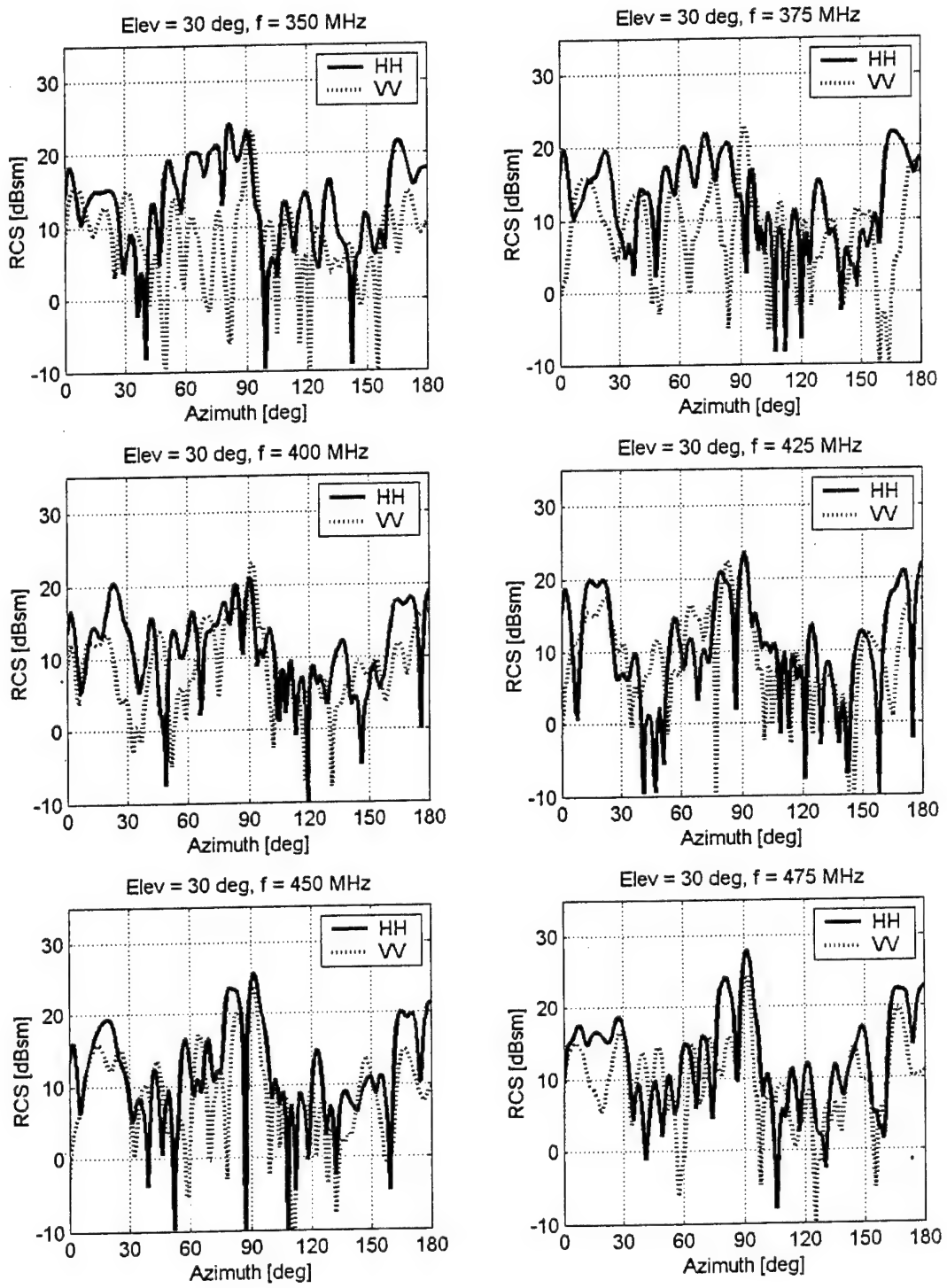
Figure 7. RCS of Full-size Tank Obtained from Model Measurements at 350, 375, 400, 425, 450, and 475 MHz

A plot of the RCS averaged over all measurement frequencies gives insight into the overall behavior of the RCS as a function of aspect angle, as shown in Figure 8 for grazing angles of 27, 30, and 33 deg. The averaging smoothes the fine structure variations and highlights the strong dependence of the RCS on aspect angle. The 3 – 5 dB greater broadside RCS of HH compared to VV polarization is clear. An even greater difference occurs for the end-on aspects. Here, there can be a 5 – 10 dB difference between HH and VV polarizations.

There are small changes in the RCS level of the broadside and the head-on returns over the grazing angle range. The tail-on aspect does show considerable change in the HH component manifested chiefly in the spreading of a higher RCS region over a wider range of angles. This same broadening trend is also apparent for broadside aspects.

In the absence of foreground multipath, the variation of RCS with grazing angle depends on the main scattering lobe width $\theta \approx \lambda/D$ where λ is the wavelength and D the extent of the object in the observation plane. For a tank of roughly 3 x 3 x 8 m on a side illuminated by a radar operating at a center frequency of 300 MHz, this translates into broadside scattering lobe widths of about 20 deg and 7 deg in the elevation and azimuth planes, respectively. Thus, we see more variation in RCS as a function of aspect angle than for a similar change in grazing angle, as expected.

5.2   UHF ISAR Images of a Tank

An advantage, already cited, of collecting data by rotating the target past the radar is that images at any aspect can be constructed with the data collected from one run. The images in this section were generated by integrating over a ±18 deg range of azimuth angles centered on the aspect for which the image was computed. The frequency samples used to generate these images scaled from 201 to 444 MHz in steps of 1.34 MHz. These values of integration angle and bandwidth result in cross-range and down-range resolutions of about 1 m and 0.7 m, respectively. To save time, we collected data over the limited azimuth range of 0 – 180 deg. Because the tank is not symmetrical about its longitudinal axis, we do not process images near the end-on aspects where data are lacking. The processing imposes a 20 dB Kaiser taper on the frequency and azimuth angle data samples to decrease processing artifacts in the images at the cost of decreased resolution. Finally, we have referenced the intensities of all images to the same level so we can compare the intensity variations among the images with aspect and grazing angle directly.

The images that result are shown in Figure 9 for a 27-degree grazing angle. Comparison of these with the photographs in Figure 5 helps to identify the scattering centers of the target. The bright regions in the photographs are areas where strong direct or multipath reflections occur. In Figure 9 and the other image figures that follow, individual images are plotted in a target-centered system. That is, one in which the target is fixed and the radar moves around the target. As further clarification, the tank, shown in outline form in each of the plots, always points directly up toward the top of the page independent of the aspect angle giving the relative bearing between the tank heading and the radar line-of-sight. Because of this plotting geometry, the cross-range direction is always normal to the radar line-of-sight and the down-range direction is always along the radar line-of-sight. Also in these images, the tank's gun is parallel to the ground and oriented about 5 degrees to the right of the forward direction.

Frequency Averaged RCS at 27 deg Elevation

Frequency Averaged RCS at 30 deg Elevation

Frequency Averaged RCS at 33 deg Elevation
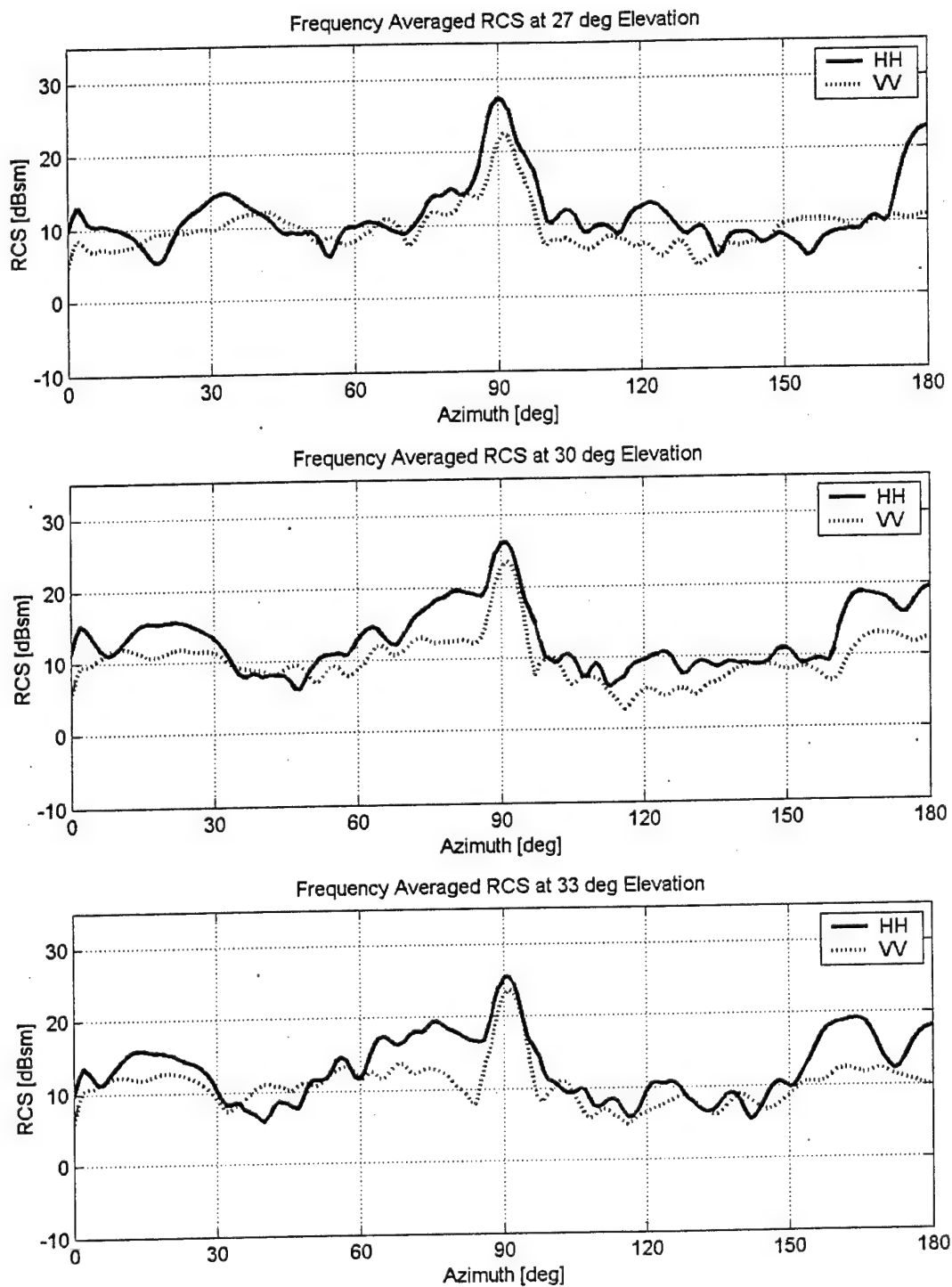
Figure 8. Frequency Averaged RCS of Full-size Tank Obtained from Model Measurements

The resolution of these images, about 1.0 x 0.7 m, does not provide an easily recognizable outline of the target. Even so, a rough estimate of the target's length and width can sometimes be made. The broadside image pixel intensities are larger than for the other poses and extend over a longer cross-range dimension. The large change in the distribution and intensity of the image pixels with aspect angle is apparent from the plots. Often, the image shows in front of the target outline as in the 90-deg aspect image. This is because scattering centers at the same ground range exhibit shorter slant ranges in inverse proportion to their heights above the ground. Thus, the top of the tank is at a shorter range than the bottom of the tank. Therefore, the pixels associated with this shorter range will be displayed at shorter range before those due to scattering originating from lower on the tank. By the same reasoning, the pixel due to the single-bounce multipath contribution will be displayed at a longer range than the direct-path contribution from the same point on the tank. In fact, for the single-bounce dihedral, the apparent scattering center position is the vertex of the dihedral at the base of the target object, i.e., at the true ground range of that scattering center. The double-bounce contribution is delayed even more.

The images for VV polarization for 27-degree grazing angle are shown in Figure 10. The pixel intensities tend to be smaller than and their distribution substantially different from those of HH polarization image. This is because the amplitudes and phases of scattered signals and their interaction with the multipath signals are different for the two polarizations.

In Figures 11 and 12 we show the HH and VV images of the tank for a 30-deg grazing angles. There are significant differences between the HH and VV images. And again, the intensities of the HH image tend to be greater than for VV polarization. The images for a 33-deg grazing angle in Figures 13 and 14 show similar differences. The HH images tend to display higher intensity levels than the VV images.

As expected, there are large differences in the image structures with aspect angle. Also, there are large differences in the image structure for small (±3 degrees) changes in elevation angle or grazing angle. The significance of the rapid changes in the images with grazing angle is that classification and/or identification algorithms must be able to accommodate the rapid variation in a target's image with even small changes in grazing angle.

We computed the correlation coefficients, referenced to the image for 30 deg elevation, of the complex and intensity image arrays as a function of grazing angle. The results are shown in Figure 15. The correlation coefficients of the complex voltage and intensity image arrays fall off on both sides of the reference angle and drop to about 0.7 and 0.8, respectively, for elevation angle changes of ±3 deg.

Had the grazing angle been near the Brewster angle, about 14 deg, the variation in the images with grazing angle would have been less for VV polarization because the intensity of the multipath component would have been too small to interfere with the direct components. For dry soil conditions, the Brewster angle is about 30 deg, right in the grazing angle region where many SARs in this frequency range operate.

HH, Az = 30°, El = 27°

HH, Az = 60°, El = 27°

HH, Az = 90°, El = 27°

HH, Az = 120°, El = 27°

HH, Az = 150°, El = 27°

f = 201 to 444, every 1.34 MHz
ϕ = -18 to 18, every 1 deg
Taper: 20 dB Kaiser
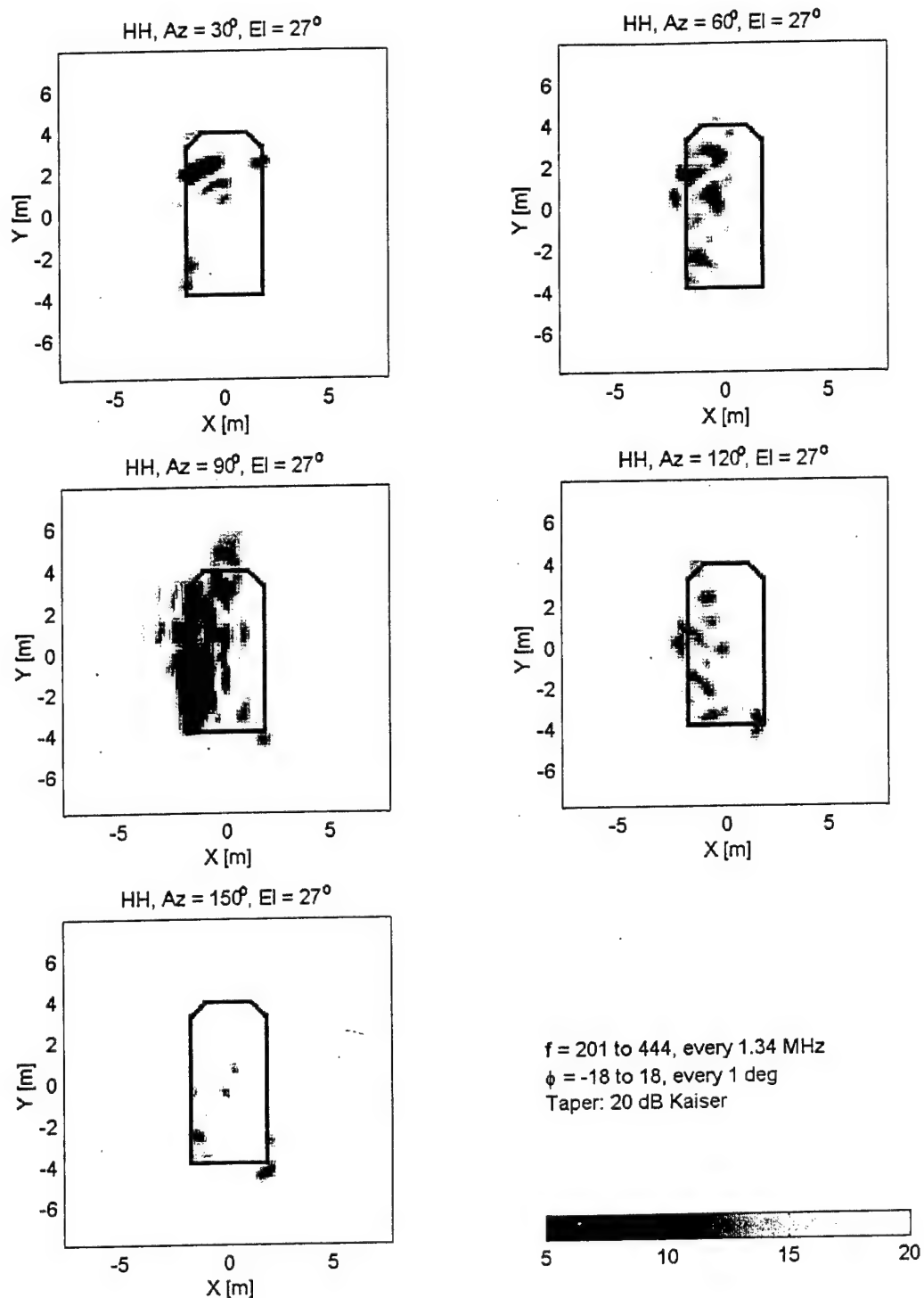
Figure 9. ISAR Images of a Tank for Aspect Angles of 30, 60, 90, 120, and 150 Degrees; HH Polarization; and a 27-Degree Grazing Angle

14

VV, Az = 30°, El = 27°

VV, Az = 60°, El = 27°

VV, Az = 90°, El = 27°

VV, Az = 120°, El = 27°

VV, Az = 150°, El = 27°
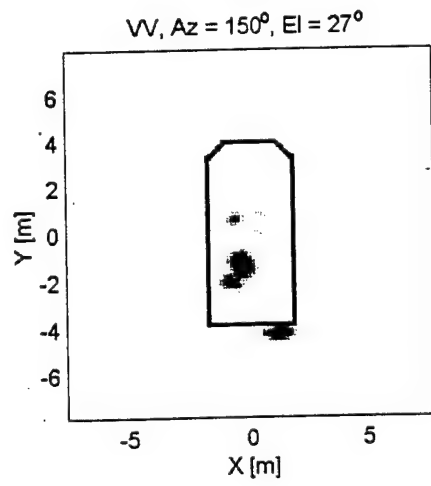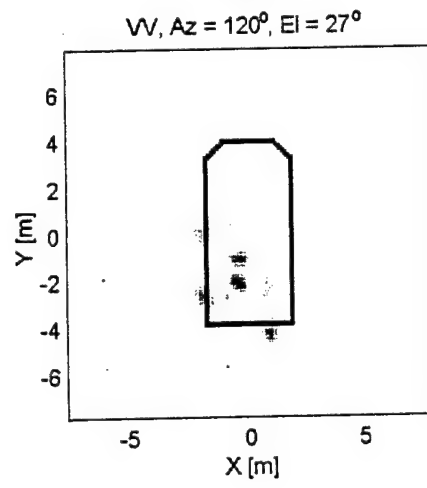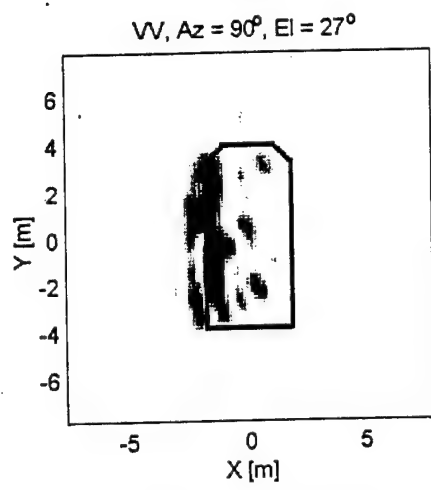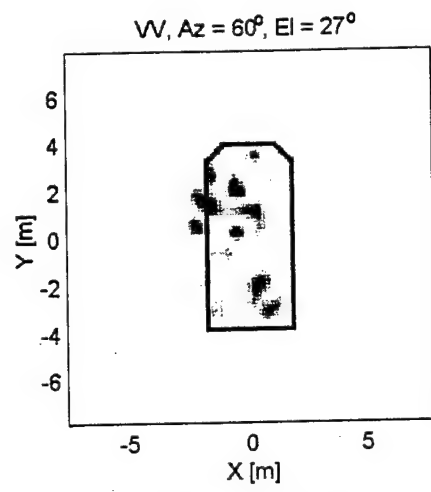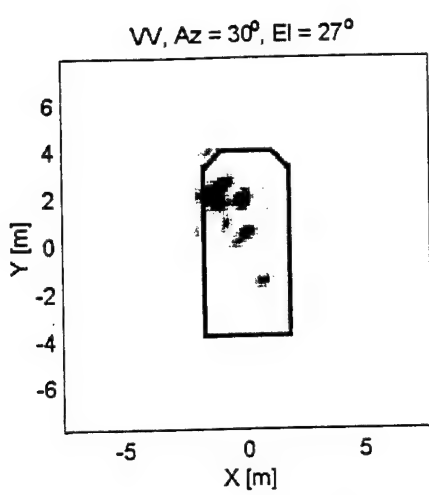
f = 201 to 444, every 1.34 MHz
φ = -18 to 18, every 1 deg
Taper: 20 dB Kaiser

Figure 10. ISAR Images of a Tank for Aspect Angles of 30, 60, 90, 120, and 150 Degrees; VV Polarization; and a 27-Degree Grazing Angle

15

HH, Az = 30°, El = 30°

HH, Az = 60°, El = 30°

HH, Az = 90°, El = 30°

HH, Az = 120°, El = 30°

HH, Az = 150°, El = 30°

f = 201 to 444, every 1.34 MHz
φ = -18 to 18, every 1 deg
Taper: 20 dB Kaiser

5   10   15   20
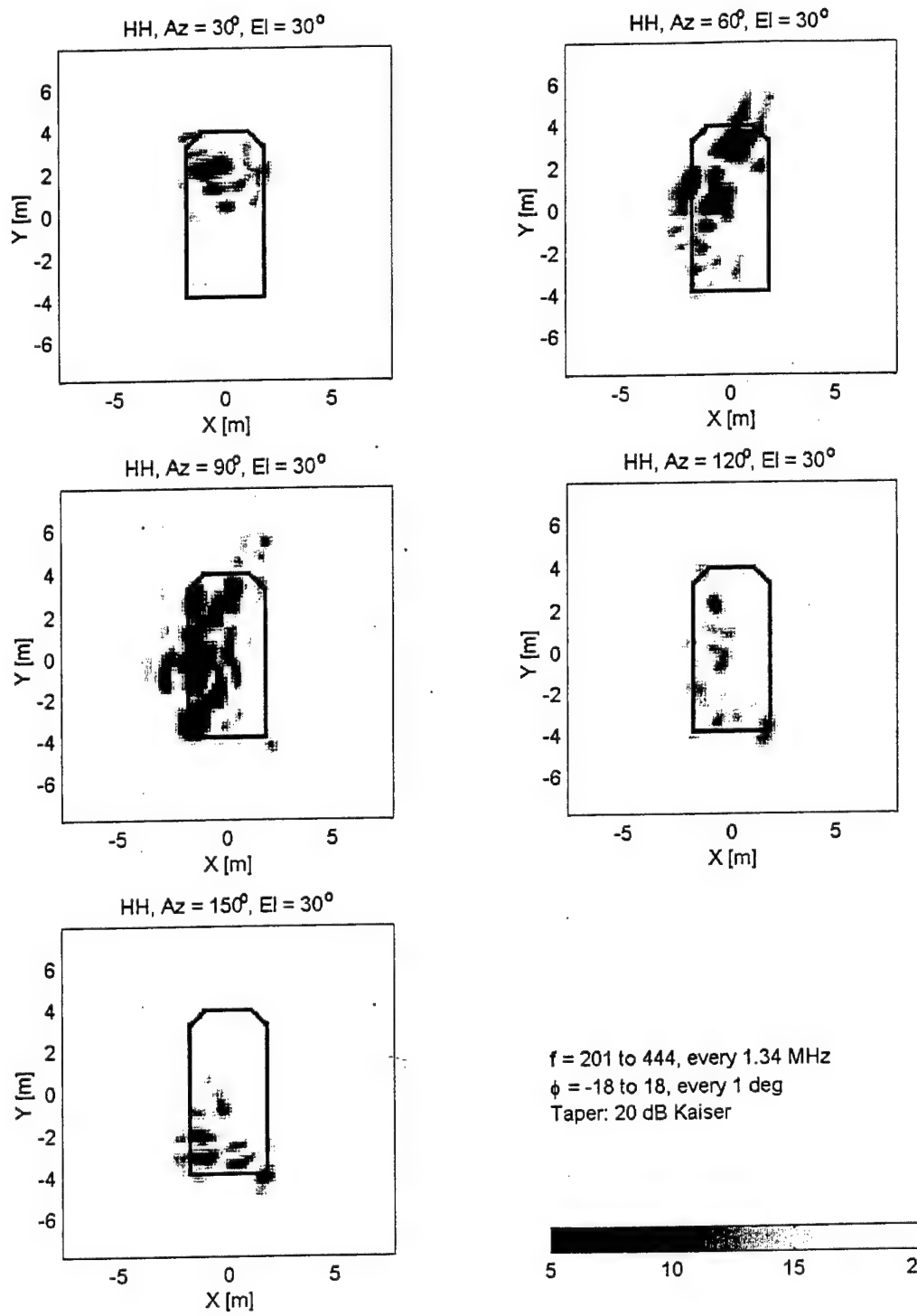
Figure 11. ISAR Images of a Tank for Aspect Angles of 30, 60, 90, 120, and 150 Degrees; HH Polarization; and a 30-Degree Grazing Angle

16
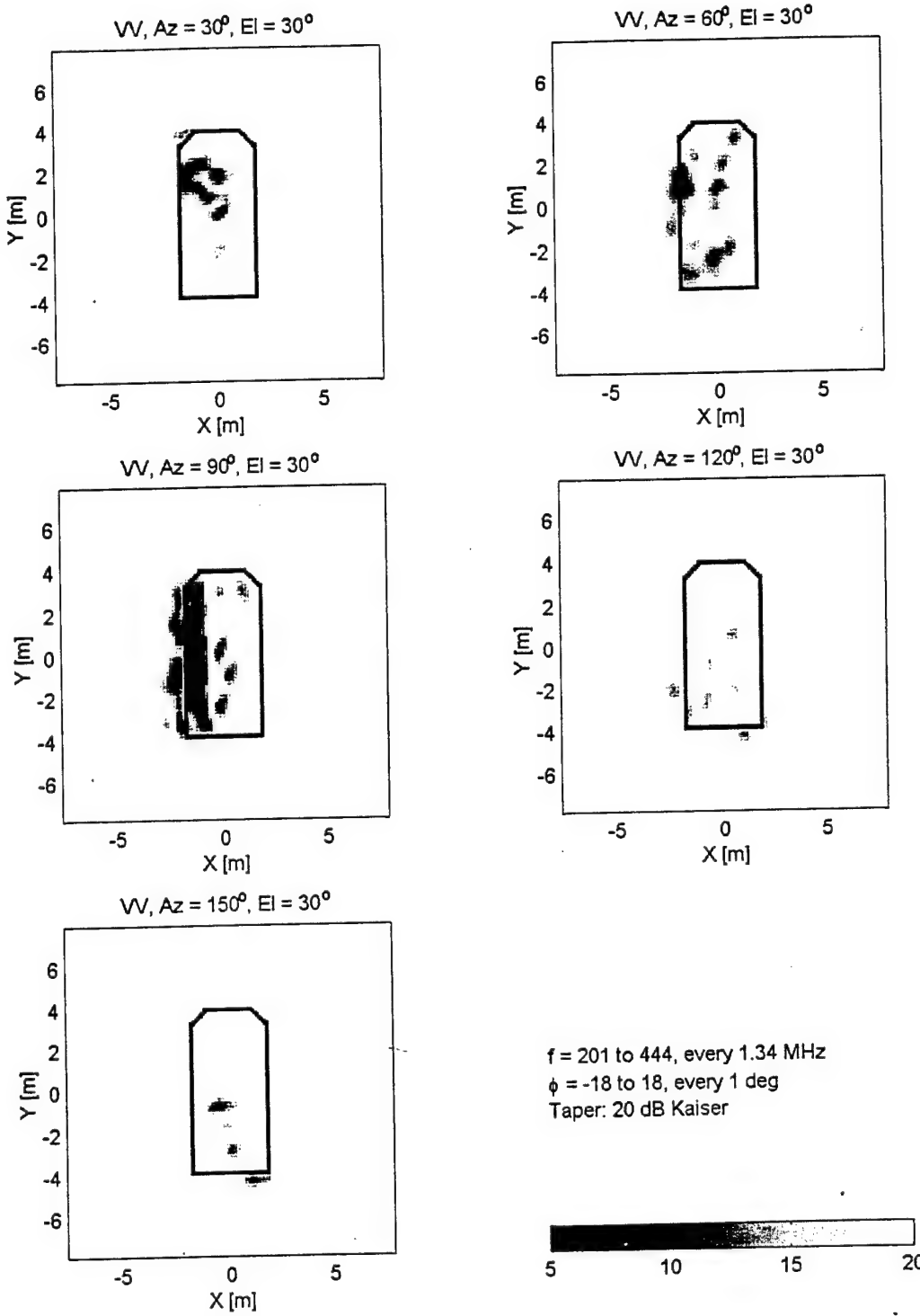
Figure 12. ISAR Images of a Tank for Aspect Angles of 30, 60, 90, 120, and 150 Degrees; VV Polarization; and a 30-Degree Grazing Angle

17
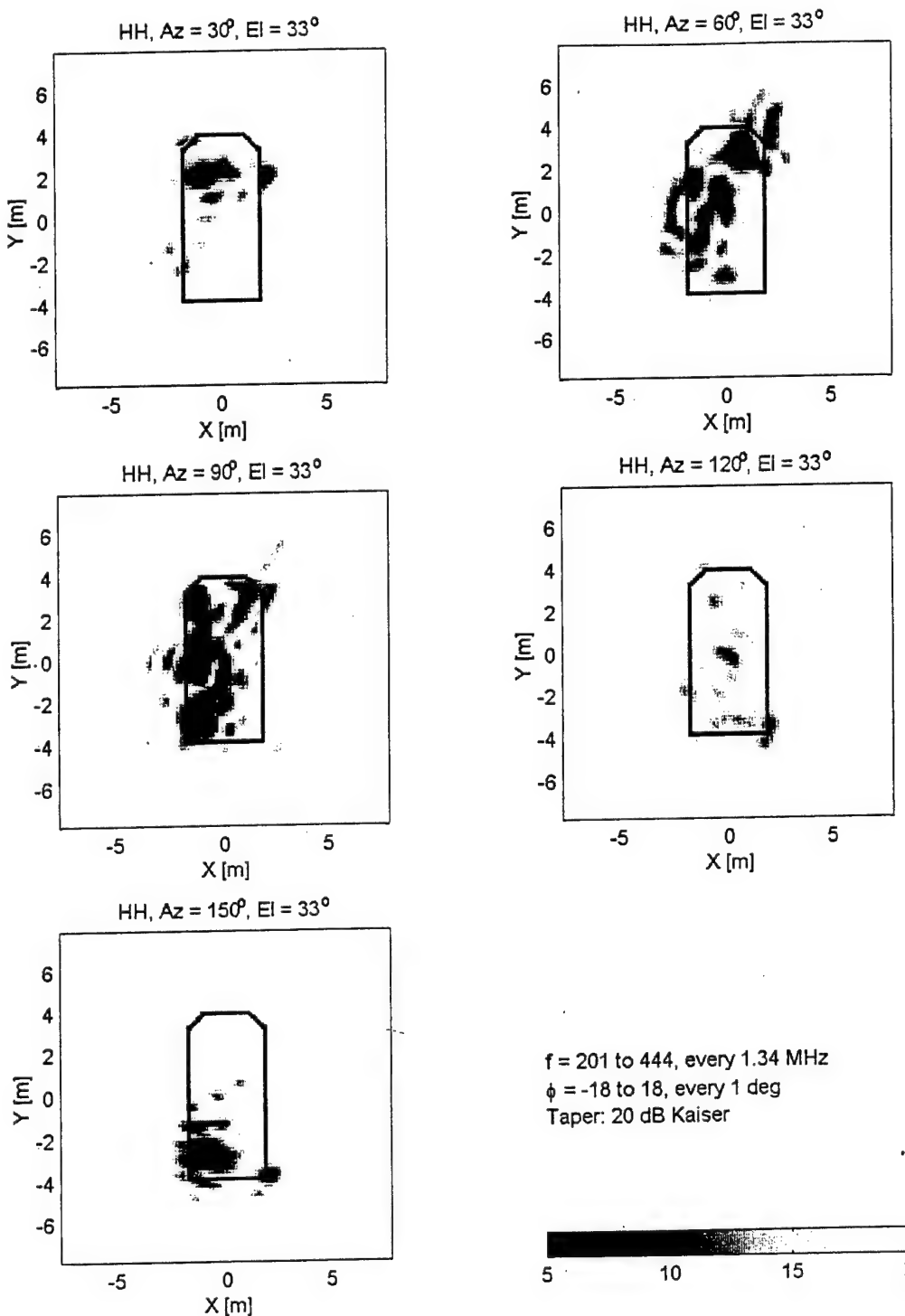
Figure 13. ISAR Images of a Tank for Aspect Angles of 30, 60, 90, 120, and 150 Degrees; HH Polarization; and a 33-Degree Grazing Angle

18
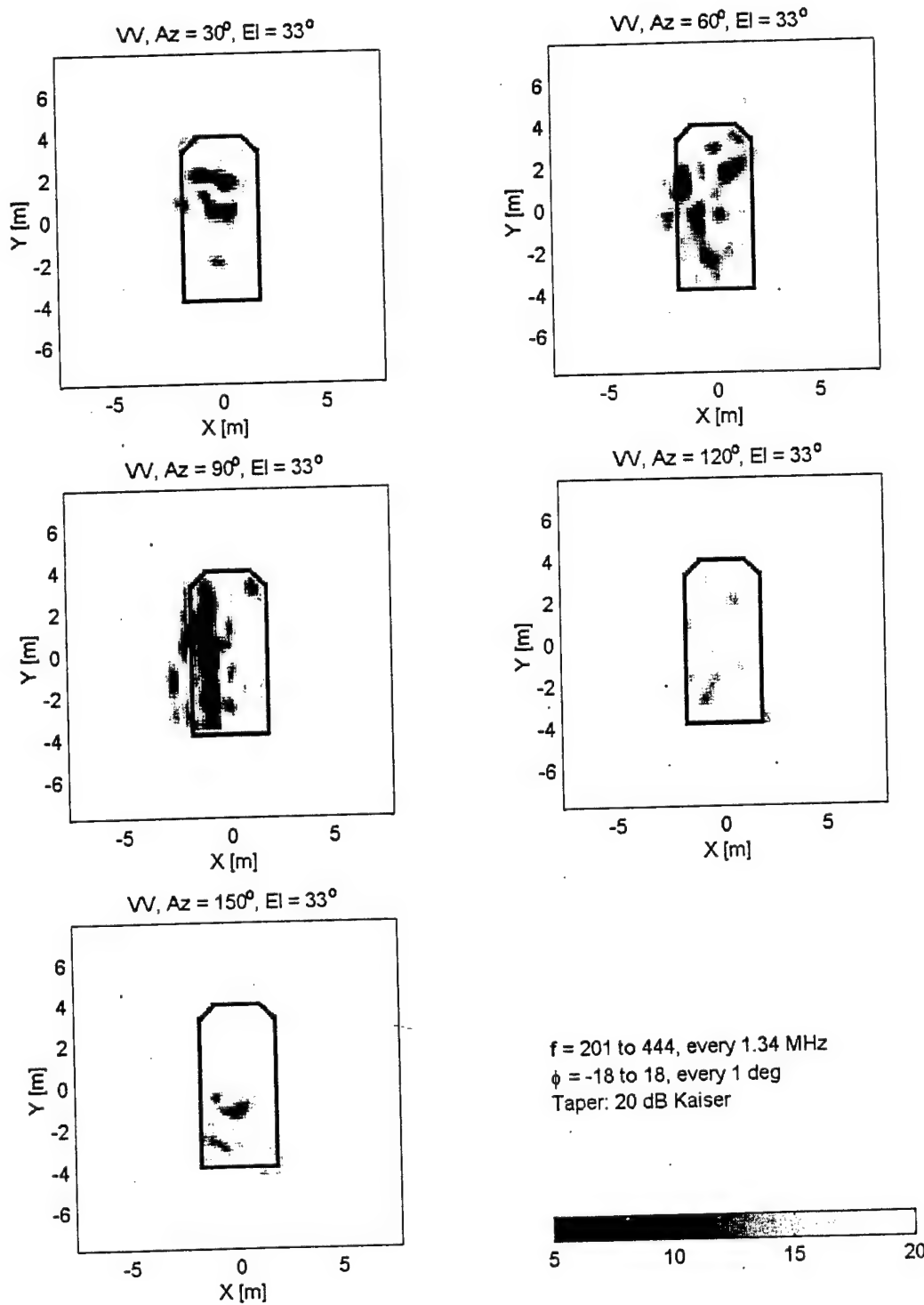
Figure 14. ISAR Images of a Tank for Aspect Angles of 30, 60, 90, 120, and 150 Degrees; VV
Polarization; and a 33-Degree Grazing Angle

19
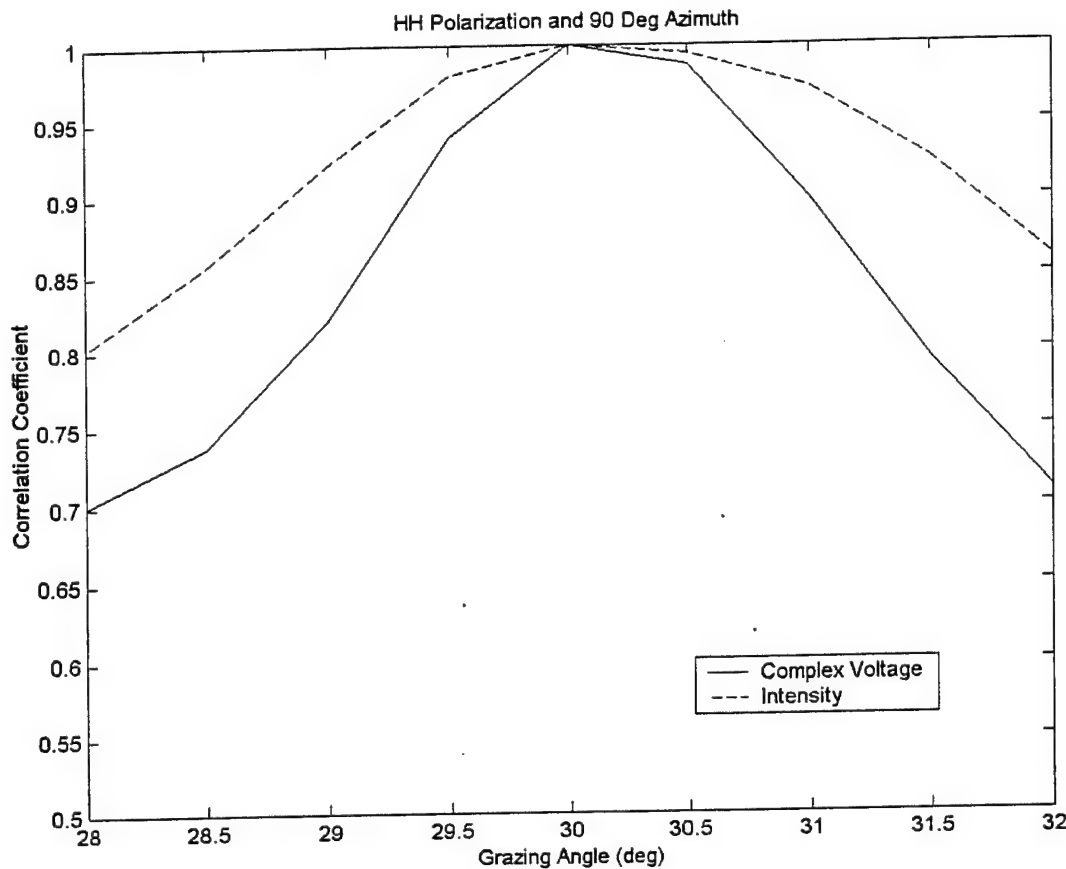
Figure 15. Image Correlation Coefficient as a Function of Elevation Angle

6. COMPARISON OF ISAR AND STRIP SAR IMAGES

In this section, we examine the differences between a laboratory ISAR image and one obtained from a linear strip SAR radar, the mode most used by operational radars. A strip-mode SAR flies along a straight path periodically sampling radar returns from the side-looking direction. The flight path length over which samples are coherently combined to form the synthetic aperture determines the cross-range resolution of the radar. Typical cross-range values for VHF and UHF radars are 3-6 and 0.5-1 meters, respectively. The cross- and down-range resolutions are usually selected to form an approximately square resolution cell. To be more useful in providing images to develop target discrimination and classification techniques, the laboratory ISAR images should be cast into strip-SAR format.

Several geometrical factors, illustrated in Figure 16, may make the image of a target produced by a linear strip SAR differ from the ISAR image of the same target obtained from turntable or scale-model measurements. For example, the depression (grazing) angle $\theta_{depression}$ of the line-of-sight from the strip SAR's real antenna to the target varies as a function of the radar's position along its flight path. For a broadside looking SAR, the depression angle is greatest at the center of the synthetic aperture (point of closest approach) and decreases toward the ends of the synthetic aperture. Typical variations in grazing angle are 3 – 5 degrees. Although small, the

20

change, as is shown in Figures 9-14, is large enough to significantly alter the relative phases between the direct and multipath components thereby producing potentially large changes in the pixel intensities between the ISAR and strip-SAR images. An expression for $\theta_{depression}$, the strip SAR's depression angle (Figure 15), as a function φ is

$$\theta_{depression} = \tan^{-1}[\tan\theta_o \cos\varphi], \qquad (1)$$

where θ_o is the scale-model or turntable grazing angle at the point of closest approach and φ is the azimuth of the ground range line measured from the same line at the point of closest approach. For a radar at 3000 m altitude, a grazing angle of 30 deg at the point of closest approach, and a half-aperture angle of 30 deg, the grazing angle at the edge of the synthetic aperture is about 26.6 deg, which is 3.4 deg less than at the point of closest approach. The change in grazing angle for several starting grazing angles is plotted in Figure 17. The change in grazing angle increases as the central grazing angle becomes larger. For a central grazing angle of 45 deg, the grazing angle decreases by more than 4 deg over the aperture, enough to produce substantial changes in target images.
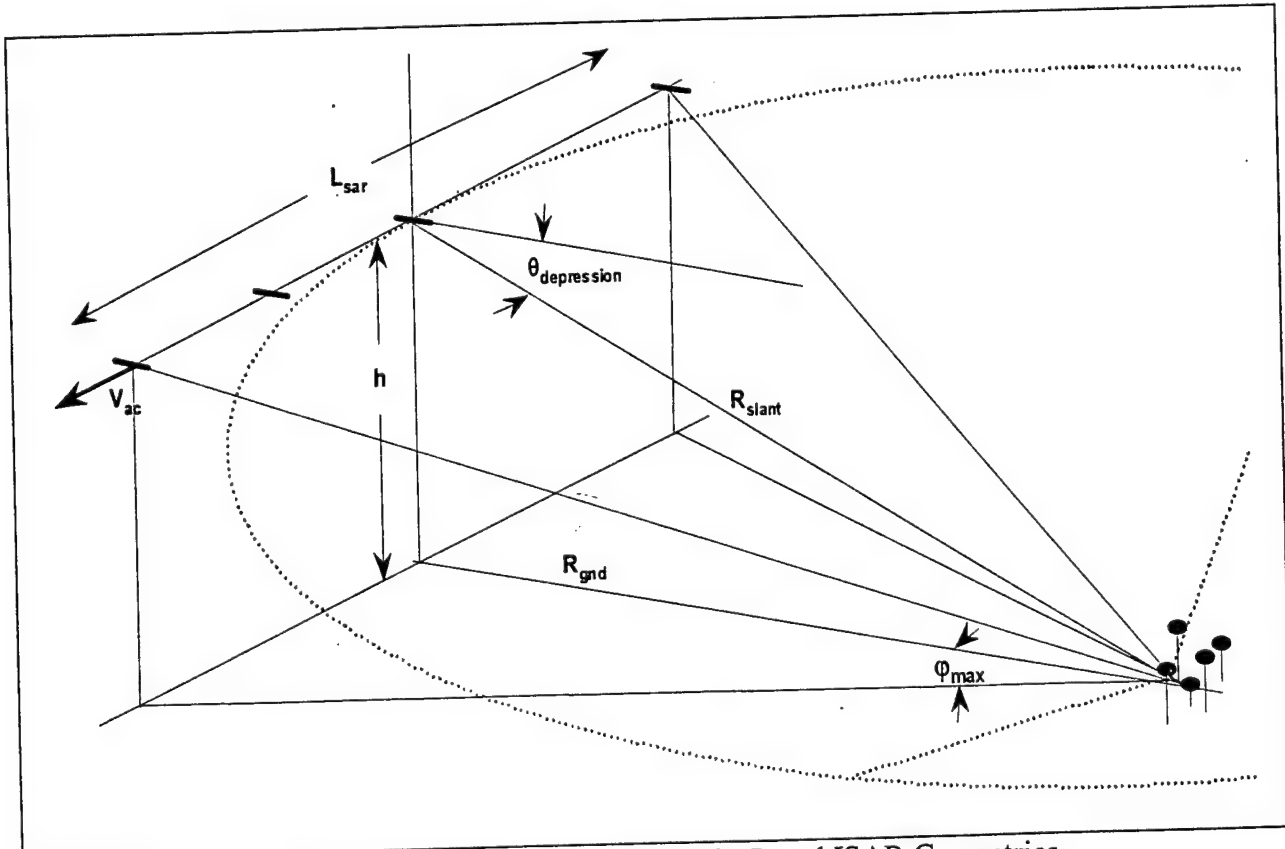

Figure 16. Comparison of Strip SAR and ISAR Geometries
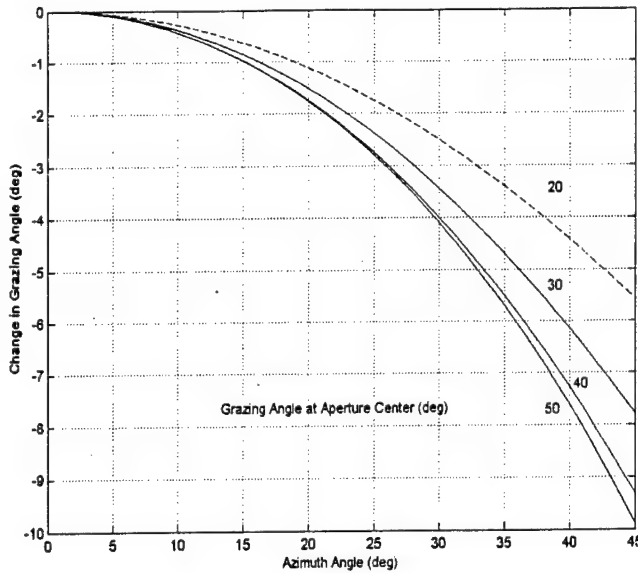
Figure 17. Grazing Angle versus Synthetic Aperture Angle Azimuth SAR

Another source of differences between ISAR and strip-SAR images is that the strip SAR real antenna gain falls off toward the edges of the synthetic aperture because its antenna pointing direction is fixed. For scale-model and turntable ISAR measurements, the antenna gain remains constant because the antenna always points directly toward the target as the target and its ground plane rotate. The decrease in the two-way antenna gain with position along the synthetic aperture and, indeed, any phase variation due to the antenna are easily computed from knowledge of the real antenna's radiation pattern. For a horizontally or vertically polarized real antenna, the signal incident on the target remains horizontally or vertically polarized, respectively, along the SAR's flight path as does the polarization of the incident field in model or turntable measurements. Thus no correction is needed for polarization. The phase changes produced by the changing path length from the SAR to the target are routinely corrected in a focused SAR and do not have to be accounted for as a separate correction.

Finally, the free-space loss increases toward the edges of the strip SAR because the range to the target increases for aircraft positions away from the point of closest approach to the target. In scale-model and turntable measurements, the range to the target remains constant because of the circular geometry of the measurement apparatus. The range R_{slant} from the target to the real antenna as a function of the synthetic aperture's half angle is

$$R_{slant} = h \sqrt{1 + \frac{1}{\tan^2 \theta_{depression} \cos^2 \varphi}} , \qquad (2)$$

where h is the strip-SAR aperture altitude above the ground. For the example above, the added two-way free space loss is about 1.9 dB at the edges of the synthetic aperture.

22

We can take these geometrical differences between the two SAR modes into account in converting the ISAR image into an equivalent strip SAR image. The changes in antenna gain and free-space loss are often not significant because of the tapers used to reduce processing sidelobes used in computing an image. But if needed, the relative change in signal intensity produced by these two factors can be used to modify the scale-model measurement intensities to make them vary as they would in a strip-mode SAR.

Accounting for the variation in depression angle $\theta_{depression}$, although more involved, is also straightforward. We can use two techniques. In the first, the depression angle of the strip SAR is calculated as a function of the radar's flight path position. During the scale-model measurement run, the depression angle of the ground plane is adjusted to match the strip SAR depression angle as a function of ground plane azimuth φ. Since the scale-model measurement system is under computer control, we can program the necessary stage angle commands into the system before data collection. Although this approach is simple and direct, its drawback is that, just as in the case of the strip SAR, the measured data will yield an image at only the single aspect angle to which the ground plane tilt was matched.

The second method, the one we used, does not change the tilt angle during a run. Instead, several 360-degree azimuth rotation runs (we did only 0 –180 deg) are made at closely spaced (typically 0.5 deg) depression angles over the range of depression angles appropriate for the strip SAR being modeled. The data collection is phase coherent among all the depression angles measured.

The ISAR data is collected at uniformly spaced azimuth angles, usually 1 deg, and a constant grazing angle and range. The strip SAR data is collected at uniformly spaced intervals along the flight path over which the grazing angle and range change slowly. To convert the ISAR data into strip SAR format, we first calculate the azimuth and grazing angles for each uniformly spaced strip SAR collection point. Then we extract the complex field data for these by interpolating the nearest neighbor values of the ISAR data. The strip SAR image is formed from this interpolated data. The advantage of this approach is that although more test runs were required, images at any aspect angle can be obtained from the ISAR data.

The results of the conversion of an ISAR image to a strip SAR format image for $\theta_o = 30$ deg and $\varphi_{max} = \pm 18$ deg are shown in Figure 18. Three images are shown. The 30-deg image is the ISAR image at the center (30-deg elevation) of the synthetic aperture. The 28.5-deg image is the ISAR image for the grazing angle at the edges of the synthetic aperture. There is a marked difference between these two images. The linear SAR image is computed from ISAR returns for grazing angles that range 28.5 at the edges to 30 at the center. However, as shown in Figure 16, most of the samples come from images near 30 deg grazing angle. The taper to reduce processing artifacts further reduces the impact of the lower grazing angle contributions near the synthetic aperture edges. Thus the linear SAR and ISAR images do not appear very different from one another.

However, differences between linear SAR and ISAR images increase with central elevation angle and synthetic aperture length. Figure 19 shows the ISAR images and the derived linear SAR image for the same central grazing angle, 30 degrees, as the previous case but for a longer synthetic aperture, $\varphi_{max} = \pm 24$ deg. As anticipated, there is more difference between the two.

23
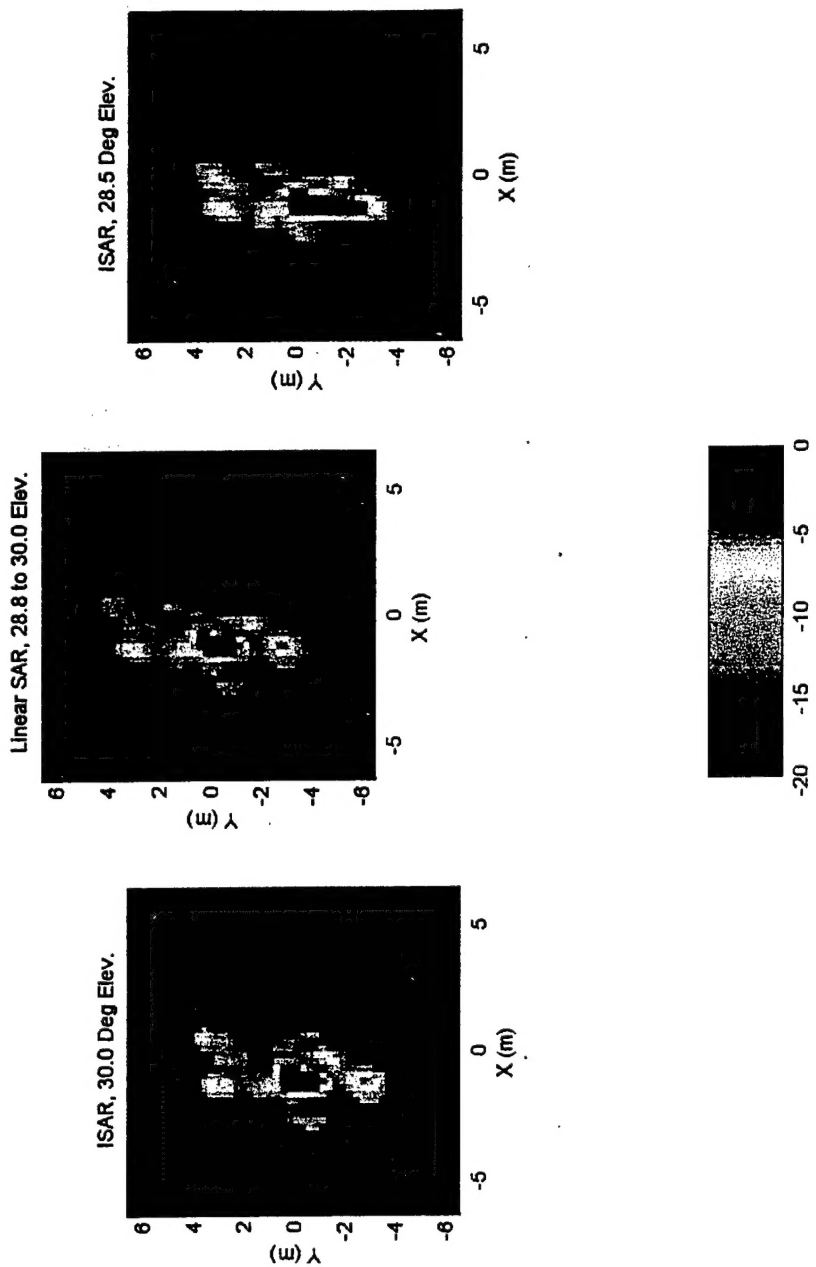
Figure 18. Comparison of Broadside ISAR and Derived Linear SAR Images. HH polarization, $\theta_o = 30$ deg , and $\varphi_{max} = \pm18$ deg. For use in Table 1, the images are named from bottom to top: Central, Linear, and Edge.
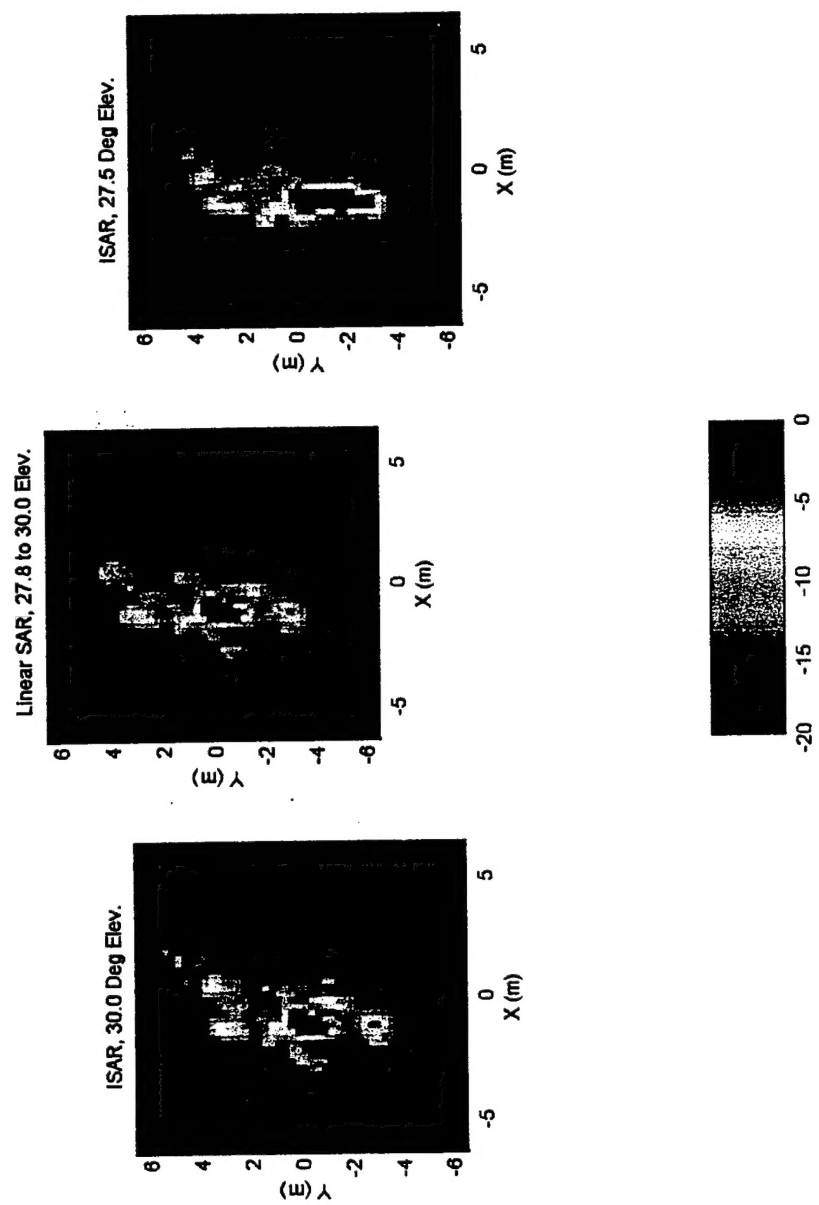
Figure 19. Comparison of ISAR and Derived Linear SAR Images. HH polarization, $\theta_o = 30$ deg, and $\varphi_{max} = \pm 24$ deg. . For use in Table 1, the images are named from bottom to top: Central, Linear, and Edge.

Table 1 lists the correlation coefficients among the images shown in Figure 18 and in Figure19 and displays the greater differences between the central ISAR images and the derived linear SAR images as the aperture width increases.

Table 1. Correlation Coefficients of ISAR and Derived Linear Images. For a 30-deg central grazing angle and a 90-deg azimuth target aspect angle. Central – ISAR image at 90 deg aspect; Linear – SAR image at 90 deg aspect; Edge – ISAR image at edge aspect of the synthetic aperture.

$\Delta\varphi$ (deg)	Image Pair	Correlation Type	Correlation Coefficient
± 18	Central –Linear	Voltage	0.93
		Intensity	0.99
	Central – Edge	Voltage	0.74
		Intensity	0.86
	Edge – Linear	Voltage	0.81
		Intensity	0.88
± 24	Central – Linear	Voltage	0.88
		Intensity	0.98
	Central – Edge	Voltage	0.62
		Intensity	0.76
	Edge – Linear	Voltage	0.64
		Intensity	0.78

7. DISCUSSION

We have shown how scale models can be used to obtain RCS and image data of full-scale targets and how ISAR images can be converted to linear SAR images.

We found that there was little difference between ISAR and derived linear SAR images for central grazing angles of 30 deg and for subtended synthetic aperture angles of 36 and 48 deg. Radars with higher central grazing angles and longer synthetic apertures would exhibit larger differences between their ISAR and linear SAR images.

However, the most important factor in scale-model measurements is the permittivity of the ground plane. It is apparent that the dielectric constant of the material under the full-scale and scale-model targets has a large impact on their effective RCS and on details of their images. For the model measurements to simulate full-scale measurements realistically, the dielectric constant of the ground plane over which the target model is measured must be reasonably close to that of the terrain over which the full-scale target details are desired. For rough terrain, roughness must also be introduced into the ground plane. Neither of these factors is a problem. Materials are available to produce ground planes with a broad range of permittivity that simulate dry to wet soils. Roughness features have been added to the smooth surface of a ground plane during fabrication, as well. We examine rough terrain in future work.

References

1. Currie, Nicholas C., Editor, *Radar Reflectivity Measurement Techniques and Applications*, Artech House, Boston, London 1989

2. Sinclair, George, "Theory of Models of Electromagnetic Systems," PROC. IRE, pp. 1364-1370, Nov. 1948

3. Giles, R.H, Gatesman, A. J., Fitz-Gerald, J., Fisk, S. and Waldman, J. "Tailoring Artificial Dielectric Materials at Terahertz /Frequencies," The Fourth International Symposium on Space Terahertz Technology, April 1993, Los Angeles, CA

4. Bober, Kenneth M., Giles, Robert H, and Waldman, Jerry "Tailoring The Microwave Permittivity And Permeability Of Composite Materials," Submillimeter-Wave Technology Center, University of Massachusetts, Lowell, MA

5. Beaudoin, Christopher J., "Development of a 1/35th Scale VHF/UHF Far-Field RCS imaging System Used To Investigate Scattering and Imagery of Tree Obscured Targets," Master of Science Thesis, Dept. of Electrical Engineering, University of Massachusetts, Lowell, MA